International Journal of Multiphase Flow 142 (2021) 103720

Contents lists available at ScienceDirect

International Journal of Multiphase Flow

journal homepage: www.elsevier.com/locate/ijmulflow

Transonic flow focusing: stability analysis and jet diameter

M. Rubio[a], A. Rubio[a], M.G. Cabezas[a], M.A. Herrada[b], A.M. Gañán-Calvo[b], J.M. Montanero[a,*]

[a] Departamento de Ingeniería Mecánica, Energética y de los Materiales and Instituto de Computación Científica Avanzada (ICCAEx), Universidad de Extremadura, Badajoz E-06006, Spain
[b] Departamento de Ingeniería Aerospacial y Mecánica de Fluidos, Universidad de Sevilla, Camino de los Descubrimientos s/n 41092, Spain

ARTICLE INFO

Article history:
Received 26 April 2021
Revised 1 June 2021
Accepted 2 June 2021
Available online 8 June 2021

Keywords:
Flow focusing
Global stability
Serial femtosecond crystallography

ABSTRACT

We study numerically and experimentally the stability of the transonic flow focusing used in serial femtosecond crystallography (SFX) to place complex biochemical species into the beam focus. Both the numerical and experimental results indicate that the minimum flow rate for steady jetting increases slightly with the gas stagnation pressure. There is a remarkable agreement between the stability limit predicted by the global stability analysis and that obtained experimentally. Our simulations show that the steady jetting interruption at the critical flow rate is caused by the growth of a perturbation with a constant phase shift. This result is consistent with the experimental observations, which indicate that both the meniscus tip and the emitted jet collapse almost simultaneously at the stability limit. We derive a scaling law for the jet diameter as a function of the liquid flow rate and gas density/pressure from more than one hundred simulations. The scaling law provides accurate predictions for the jet diameter within the range of values [0.549,10.9] μm analyzed in this work.

1. Introduction

In the original gaseous flow focusing configuration (Gañán Calvo, 1998), the liquid is injected at a constant flow rate Q_l across a feeding capillary placed in front of a discharge orifice whose diameter is commensurate with that of the capillary. A high-speed gaseous stream coflows with the liquid across the discharge orifice. The pressure drop Δp and viscous shear stress caused by the gaseous current drives the liquid flow, while the energy transferred to the system by injecting the liquid at the flow rate Q_l is negligible. A very thin jet tapers from the tip of the meniscus attached to the edge of the feeding capillary. DePonte et al. (2008) modified the original plate-orifice flow focusing configuration (Gañán Calvo, 1998) by introducing the feeding capillary in a fire-shaped nozzle to produce the focusing effect. They coined the expression "Gas Dynamic Virtual Nozzle" (GDVN) to refer to this ejector. Gaseous flow focusing is a paradigmatic example of tip streaming (Montanero and Gañán Calvo, 2020) used in multiple applications.

In the incompressible regime, and neglecting the role of both surface tension and viscosity in the liquid and gas phases, the jet diameter d_j in the two configurations can be calculated as (Gañán Calvo, 1998)

$$d_j = \left(\frac{8\rho_l Q_l^2}{\pi^2 \Delta p}\right)^{1/4}, \tag{1}$$

where ρ_l is the liquid density. The viscous shear stress exerted by the gaseous stream on the liquid surface transfers axial momentum to the jet and can significantly reduce its diameter below the inviscid approximation (1). This approximation can be improved by considering the viscous drag force both in the discharge orifice and beyond it (Gañán Calvo et al., 2011). To the best of our knowledge, a scaling law for the jet diameter (speed) has not yet been derived for the compressible (transonic) regime.

The serial femtosecond crystallography (SFX) is probably the most important gaseous flow focusing application. In SFX, complex biochemical species are analyzed by recording single flash diffraction patterns of many individual protein crystals (Chapman et al., 2011). X-ray free-electron lasers (XFELs) produce flashes sufficiently bright to generate resolvable diffraction patterns from submicron crystals. These flashes destroy the crystals, which implies that the data are to be collected from a row of crystals streaming across the X-ray beam. Most SFX experiments make use of a thin liquid jet to place the sample into the beam focus. SFX demands stringent conditions for jet emission. The jet must be at most very few microns in diameter to reduce the background diffraction signal. The jet must be long enough because the jet portion inter-

* Corresponding author.
E-mail address: jmm@unex.es (J.M. Montanero).

https://doi.org/10.1016/j.ijmultiphaseflow.2021.103720

acting with the X-ray pulse must be located sufficiently far away from the nozzle exit to avoid a rapid collection of sputtered material from the explosion. The jet must be perfectly steady to ensure a consistent interaction with the X-ray beam. Finally, the jet must be fast enough to allow the exposed sample to exit the interaction region before the next flash strikes the jet Stan et al. (2016); Wiedorn et al. (2018). To summarize, liquid jets as thin, long, steady, and fast as possible are required for the proper functioning of the SFX technique.

Gaseous flow focusing (aerodynamic focusing) (Gañán Calvo, 1998; DePonte et al., 2008; Gañán Calvo et al., 2010) with converging nozzles has been the preferred method to produce jets fulfilling the above severe constraints. The search for the best ejection conditions has led to the use of transonic and supersonic streams of helium to focus the liquid jet on one side and the optimization of the nozzle geometry (Beyerlein et al., 2015; Piotter et al., 2018; Wiedorn et al., 2018) on the other side. Different geometrical configurations have been considered to minimize/maximize the jet's diameter/speed. For instance, and following the idea proposed by Acero et al. (2013), Nazari et al. (2020) have recently used liquid feeding capillaries with syringe shape to produce jets with diameters down to 325 nm and speeds up to 170 m/s. Despite the advances mentioned above, the optimization of the liquid ejection remains an open problem due to the continuously increasing frequency of SFX repetition rates.

The gas compressibility significantly affects the outcome of flow focusing for gas velocities similar to the sound speed. Obtaining an accurate but simple scaling law to predict the jet diameter (speed) in the transonic regime is of great importance for applications such as SFX. As occurs in the incompressible regime Eq. (1), the liquid flow rate is the major factor determining the jet diameter. As the flow rate decreases, the specific energy transferred to the liquid increases, and the jet diameter/speed decreases/increases. However, the flow rate cannot be reduced without limit because the jetting regime produced by flow focusing becomes unstable for flow rates below a certain minimum value, which depends on the rest of governing parameters. Therefore, the search for the optimum liquid ejection conditions necessarily involves two aspects of the problem: (i) the maximization of the energy transmitted by the gas stream to the liquid jet, and (ii) the stabilization of the flow producing the liquid ejection. Understanding the physical mechanism responsible for the transonic flow focusing instability at the minimum flow rate has considerable implications at both the fundamental and practical levels.

Direct numerical simulations of transonic flow focusing (Zahoor et al., 2018c) have been conducted from the time integration of the Navier-Stokes equations in the laminar regime with the Volume of Fluid (VoF) method (Hirt and Nichols, 1981). These simulations have proved to constitute a useful tool for analyzing different aspects of the problem. Among the geometrical parameters analyzed in the simulations, the nozzle outlet diameter has the biggest influence on the jet diameter. In contrast, the feeding capillary angle and the capillary-to-orifice distance have a very small effect on the liquid flow (Zahoor et al., 2018a). The influence of this distance on the minimum liquid flow rate approximately follows the scaling law empirically derived by Vega et al. (2010) in the incompressible regime. Sarler et al. (2021) have recently shown that a change in angle of the nozzle outlet orifice has a significant effect on the jet emission. The influence of the gas (Zahoor et al., 2018b) and liquid (Zahoor et al., 2020) properties on the jet's characteristics has been examined from direct numerical simulations as well. Zahoor et al. (2018c) found a qualitative agreement between the scaling law (1) for the incompressible regime and their numerical results.

The calculation of the flow under steady conditions (the so-called base flow) is probably the most efficient way of determining the jet diameter. Once a numerical solution of the hydrodynamic equations has been found, the values of the governing parameters can be swept to produce systematically new numerical flow focusing realizations with relatively short computing time. In this way, one can determine the optimal conditions that maximize the energy transfer from the gas to the liquid. However, this study must be accompanied by the stability analysis of the steady solutions to verify whether those numerical realizations are physically meaningful. The global linear stability analysis (Theofilis, 2003; Chomaz, 2005; Theofilis, 2011) is probably the best procedure to fulfill that purpose. In this procedure, we calculate the eigenmodes describing the response of the base flow to small-amplitude perturbations (Theofilis, 2003; Chomaz, 2005; Theofilis, 2011). One assumes that a base flow corresponds to a true jetting realization if and only if all the eigenmodes decay on time. Cruz-Mazo et al. (2017) showed that the global stability analysis predicts reasonably well the stability of gaseous flow focusing for large applied pressure drops in the incompressible regime. This analysis has recently been extended to liquid-liquid systems (Cabezas et al., 2021) with similar conclusions. It must be noted that the calculation of the base flow and its eigenmodes does not allow one to predict the jet breakup length, which is an important parameter in applications such as SFX. That prediction requires the time integration of the hydrodynamic equations to determine where the growth of unstable perturbations gives rise to the droplet formation.

The global stability analysis of freely moving jets must be conducted carefully. The physical domain is unbounded downstream, making it necessary to impose an arbitrary cut-off in the numerical domain far away from the discharge orifice. "Soft" boundary conditions are frequently prescribed on that outlet surface. The cut-off may significantly affect eigenmodes corresponding to instabilities that originated in the emitted jet. However, and as will be shown in Sec. 5, these instabilities are subdominant in our problem, and both the cut-off length and the outlet boundary condition have a small effect on the growth rate of the dominant global mode (Tammisola et al., 2012; Gordillo et al., 2014; Augello et al., 2018). For this reason, the stability analysis is expected to be accurate for the present fluid configuration. It is worth mentioning that this may also occur in viscous capillary systems, which explains why perturbations can be forced to vanish at the outlet of those systems (Sauter and Buggisch, 2005; Tammisola et al., 2012; Rubio-Rubio et al., 2013; Augello et al., 2018).

In this paper, we study numerically and experimentally the transonic flow focusing used in SFX. In the numerical analysis, the steady base flow is obtained as a function of the liquid flow rate and gas stagnation pressure. The stability of the base flow is determined from the calculation of the linear eigenmodes. This analysis allows us to determine the parameter conditions leading to the steady jetting instability. The results are compared with the experimental measurements, and the physical mechanisms responsible for the instability are elucidated. Finally, potential applications of our numerical approach are discussed. Specifically, we derive a scaling law to estimate the jet diameter for the geometrical configuration and physical properties considered in our analysis.

2. Formulation of the problem

Consider a flow focusing realization in which a gas stream is injected from a chamber pressurized at a pressure p_0 and temperature T_0. The gas enters into a converging nozzle with an exit orifice of diameter D (Fig. 1) and discharges into a chamber connected to that orifice. The parameters governing the gas flow are the shear viscosity μ_g, the heat coefficients c_v and c_p, the thermal conductivity κ_g, the upstream stagnation temperature T_0 and pressure p_0, as well as the pressure of the gas stream at the discharge chamber exit p_e. The dilatational coefficient of viscosity λ_g is taken as

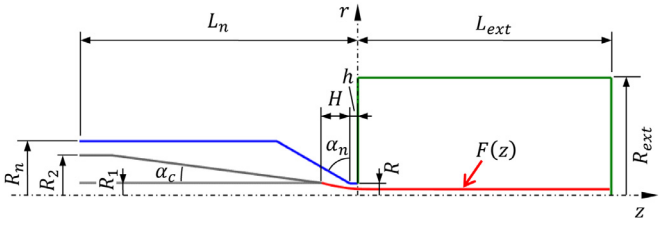

Fig. 1. Flow focusing ejector analyzed in our numerical simulations. The values of the geometrical parameters are: $R = D/2 = 35$ μm, $R_1 = D_1/2 = 37.5$ μm, $R_2 = 175$ μm, $\alpha_c = 7.5^\circ$, $R_n = 245$ μm, $h = 40$ μm, $\alpha_n = 60^\circ$, $L_n = 1260$ μm, $L_{\text{ext}} = 1260$ μm, $R_{\text{ext}} = 560$ μm. We conducted simulations for $H = 140$ μm. The function $F(z)$ represents the distance of the free surface to the symmetry axis z.

$\lambda_g = -2/3\,\mu_g$. To simplify the analysis, we neglect the influence of both the pressure and temperature on the gas properties $\{\mu_g, c_v, c_p, \kappa_g\}$. This approximation is acceptable for our purposes because (i) helium viscosity and thermal conductivity are hardly affected by the pressure (Flynn et al., 1963), and (ii) the temperature of the gas layer in contact with the liquid is practically the liquid temperature T_0, except at the nozzle exit where variations of around 10% are found (Zahoor et al., 2018a).

The gas flow drives the liquid ejection inside the nozzle. The liquid response to the aerodynamic force is determined by its density ρ_l and viscosity μ_l, the free surface tension σ, and the injected flow rate Q_l. In addition, the temperature distribution in the liquid phase depends on the thermal conductivity κ_l as well. We also neglect the influence of the temperature on the liquid properties $\{\rho_l, \mu_l, \sigma, \kappa_l\}$ because it remains practically constant in the liquid phase.

Taking into account the above considerations, and for a fixed geometry, the flow is a function of the set of dimensional parameters

$$\{D; \mu_g, c_v, c_p, \kappa_g; T_0, p_0, p_e; \rho_l, \mu_l, \sigma, \kappa_l; Q_l\}. \tag{2}$$

As can be observed, they correspond to the scale of the ejector, the physical properties of the gas, the gas control parameters, the physical properties of the liquid, and the only liquid control parameter. Both the simulations and experiments are conducted for distilled water ($\rho_l = 998$ kg/m^3, $\mu_l = 1$ mPa·s, $\kappa_l = 0.58$ W/(m·K)) and helium ($\mu_g = 0.018$ mPa·s, $c_p = 5190$ m^2/(s^{2}K), $c_v = 3120$ m^2/(s^{2}K), $\kappa_g = 0.142$ W/(m·K)). The surface tension value is $\sigma = 72$ mN/m. To reproduce the experimental conditions, we set $T_0 = 300$ K and $p_e = 75$ mbar in the simulations. The ranges of values of p_0 and Q_l in this work are similar to those typically used in SFX.

When the ratio p_0/p^* between the stagnation pressure p_0 and the hydrostatic pressure p^* at the nozzle orifice exceeds the critical value $p_0/p^* = [(\gamma+1)/2]^{\gamma/(\gamma-1)}$, the 1D isentropic gas flow becomes chocked (Shapiro, 1953). In this case, the gaseous flow in the nozzle cannot be accelerated by increasing p_0 (and keeping T_0 constant). The increase of the stagnation pressure increases the mass flow rate by raising the gas density, but it does not affect the velocity field inside the nozzle. In addition, the temperature field and, therefore, the gas viscosity do not change when the stagnation pressure is increased. This implies that the viscous stress exerted by the outer stream on the liquid current inside the nozzle remains practically constant when p_0 is increased under choking flow conditions. On the contrary, the gas density, mass flow rate, and pressure drop in the nozzle do increase with p_0. In our simulations and experiments, the 2D gaseous flow becomes chocked at the nozzle exit even for the smallest value of the upstream stagnation pressure. Therefore, the increase of that pressure hardly affects the viscous stress exerted on the free surface.

As mentioned above, one can assume as a first approximation that the gas flow is essentially governed by the control parameters $\{T_0, p_0, p_e\}$. In fact, these parameters essentially determine the force driving the liquid ejection, while the flow rate Q_l controls the response of the liquid to that force. In a second approximation, one must also consider the influence of Q_l on the gaseous flow. The liquid current moves much slower than the gas stream and acts as a still solid boundary for the gaseous flow. The liquid flow rate Q_l determines the free surface contour, and, therefore, it somehow controls the shape of the nozzle crossed by the gas stream, thus affecting all the properties of that stream. In other words, there is feedback from the liquid flow to the gas stream.

3. Governing equations and numerical method

In the simulations, we integrate the conservation equations for mass, momentum, and energy for the two phases. The general form of those equations is:

$$\frac{\partial \rho}{\partial t} + \nabla \cdot (\rho \mathbf{v}) = 0, \tag{3}$$

$$\rho \frac{D\mathbf{v}}{Dt} = -\nabla p + \nabla \cdot \boldsymbol{\tau}, \tag{4}$$

$$\rho \frac{D(c_v T)}{Dt} = -p \nabla \cdot \mathbf{v} + \boldsymbol{\tau} : \nabla \mathbf{v} - \nabla \cdot \mathbf{q}, \tag{5}$$

where $\rho(\mathbf{r}, t)$, $\mathbf{v}(\mathbf{r}, t) = v_r(\mathbf{r}, t)\mathbf{e}_r + w(\mathbf{r}, t)\mathbf{e}_z$, $p(\mathbf{r}, t)$, and $T(\mathbf{r}, t)$ are the density, velocity, pressure, and temperature fields in each phase, respectively, and D/Dt is the material derivative. These equations are completed with the constitutive relationships for the viscous stress tensor $\boldsymbol{\tau}$ and the heat flux vector $\mathbf{q}$:

$$\boldsymbol{\tau} = \mu\left(\nabla \mathbf{v} + (\nabla \mathbf{v})^{\mathrm{T}}\right) + \lambda(\nabla \cdot \mathbf{v})\mathbf{I}, \quad \mathbf{q} = -\kappa \nabla T, \tag{6}$$

where μ, λ, and κ represent the shear viscosity, dilatational coefficient of viscosity, and thermal conductivity of each phase, respectively, and $\mathbf{I}$ is the identity matrix. In addition, the equation of state $p = \rho R_g T$ is considered in the gas phase, where $R_g = c_p - c_v$ is the gas constant. We assume that the liquid is incompressible, i.e. $\nabla \cdot \mathbf{v} = 0$ in the liquid phase.

The continuity of velocity, temperature, stress and heat flux at the interface yields

$$||\mathbf{v}|| = 0, \quad ||T|| = 0, \quad \mathbf{n} \cdot ||\boldsymbol{\tau}|| - ||p||\mathbf{n} = \sigma(\nabla \cdot \mathbf{n})\mathbf{n},$$
$$||\kappa\, \partial T/\partial n|| = 0, \tag{7}$$

where $||A||$ denotes the difference between the values taken by the quantity A on the two sides of the interface, and $\mathbf{n}$ is the unit outward normal vector. The kinematic compatibility condition reads

$$\frac{\partial F}{\partial t} - v_r + w\frac{\partial F}{\partial z} = 0\,, \tag{8}$$

where $F(z, t)$ is the distance of an interface element from the axis of symmetry z.

Parabolic and uniform axial velocity profiles are imposed at the liquid and gas inlets, respectively. The mass flow rate m_0' and stagnation temperature T_0 are prescribed at the gas inlet, while the flow rate Q_l and temperature T_0 are set at the inlet of the liquid feeding capillary. The values m_0' and T_0 prescribed in the simulations can be readily translated into the governing parameters p_0 and T_0 introduced in Sec. 2. The zero-gradient (outflow) boundary condition is imposed at the gas and liquid outlets for all the variables except for the pressure whose value p_e is fixed at that section. The no-slip $\mathbf{v} = \mathbf{0}$ and no-temperature jump $T = T_0$ boundary conditions are imposed on the solid surfaces. We verified that the results are practically the same if the condition $T = T_0$ is replaced by the adiabatic wall boundary condition $\partial T/\partial n = 0$ on the solid surfaces. We did not consider the latter because it hinders

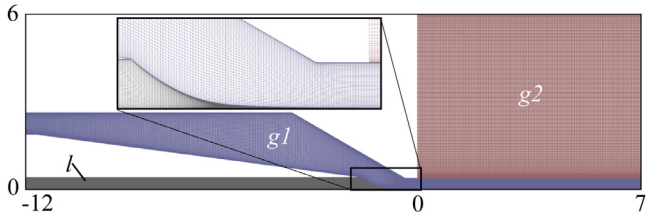

Fig. 2. Detail of the mesh used in the numerical simulations. The colors indicate the three blocks (l, $g1$ and $g2$).

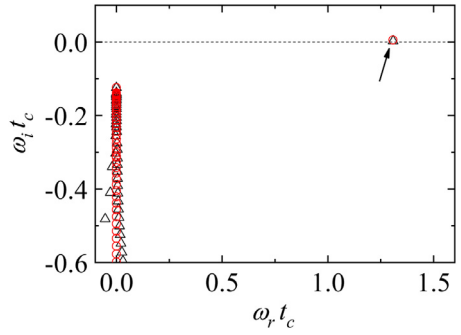

Fig. 3. Spectrum of eigenvalues for $p_0 = 1.6$ bar and $Q_l = 0.65$ ml/h calculated with $-0.1 \le \omega_r \le 1.6$ and $\omega_i > -0.7$. The circles and triangles correspond to ($n_\eta^\ell = n_\eta^{g1} = 45$, $n_\eta^{g2} = 69$, $n_\xi^\ell = n_\xi^{g1} = 859$, $n_\xi^{g2} = 313$) and ($n_\eta^\ell = n_\eta^{g1} = 51$, $n_\eta^{g2} = 79$, $n_\xi^\ell = n_\xi^{g1} = 969$, $n_\xi^{g2} = 353$), respectively. The arrow indicates the eigenvalue corresponding to the dominant mode.

the solution convergence. To complete the set of boundary conditions, we assume $\partial p/\partial n = 0$ on both the solid surfaces and the free surface.

The linear global axisymmetric modes are calculated by assuming the temporal dependence

$$\Phi(r, z; t) = \Phi_0(r, z) + \varepsilon\, \phi(r, z)\, e^{-i\omega t} \quad (\varepsilon \ll 1), \tag{9}$$

where Φ, Φ_0, and ϕ represent any hydrodynamic quantity, the base (steady) solution, and the spatial dependence of the eigenmode, respectively, while $\omega = \omega_r + i\omega_i$ is the eigenfrequency. Both the eigenmodes and corresponding eigenfrequencies are obtained as a function of the governing parameters. The dominant eigenmode is that with the largest growth factor ω_i. If that growth factor is positive, the base flow is asymptotically unstable (Theofilis, 2011). Non-axisymmetric (lateral) modes are not contemplated in our analysis because the rarefied conditions in the discharge chamber suppress the whipping instability.

The base flow and the corresponding eigenmodes are calculated with a variation of the boundary fitted method described by Herrada and Montanero (2016). A quasi-elliptic transformation (Dimakopoulos and Tsamopoulos, 2003) is applied to generate the grid (Fig. 2), which allows us to deal with the sharp reduction of the free surface radius in the meniscus tip. The equations are discretized in the transformed radial direction η using $n_\eta^\ell = n_\eta^{g1} = 45$ and $n_\eta^{g2} = 69$ Chebyshev collocation points (Khorrami, 1989) in the liquid and gas domains, respectively. The transformed axial direction ξ is discretized using fourth-order finite differences with $n_\xi^\ell = n_\xi^{g1} = 859$ and $n_\xi^{g2} = 313$ equally spaced points. The grid points accumulate near the free surface, allowing one to integrate the gaseous viscous boundary layer accurately. The simulations were run on one core of the processor Intel© Xeon© Cascade lake Platinum 8260 2.4 GHz. The base flow is calculated in around 15 min, while it takes about 50 min to obtain the eigenvalues.

Figure 3 shows the eigenvalues around the dominant one for a quasi-marginally stable base flow. The results were calculated with the grid described above and with $n_\eta^\ell = n_\eta^{g1} = 45$, $n_\eta^{g2} = 69$, $n_\xi^\ell = n_\xi^{g1} = 859$ and $n_\xi^{g2} = 313$. As can be observed, the eigenfrequency of the critical mode is practically insensitive to the grid size. The loss of stability occurs through a Hopf bifurcation ($\omega_r \neq 0$), owing to the growth of an oscillatory (periodic) perturbation. The oscillation frequency is commensurate with the inverse of the inertio-capillary time $t_c = [\rho_l D_1^3/(8\sigma)]^{1/2}$ defined in terms of the feeding capillary diameter D_1. This result suggests that the perturbation responsible for the instability affects the emitted jet and the liquid meniscus.

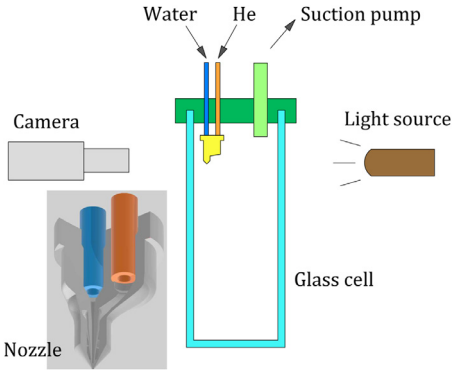

Fig. 4. Main elements of the experimental setup.

4. Experimental method

We fabricated the flow focusing ejector used in our experiments. The design was inspired by the devices developed by Knoska et al. (2020), modifying the nozzle tip and porting region to suit our requirements (Fig. 4). The nozzle was printed using Nanoscribe Photonic Professional GT2 with the Dip-in Laser Lithography (DiLL) configuration, dipping the 25× objective into the IP-S resin droplet on an ITO coated glass substrate. We chose the shell and scaffolds writing strategy and produced a 20 μm thickness shell delimiting the structure and an internal scaffold to stabilize the structure. The writing time was 35 h. The part was developed in ~25 ml of PGMEA for one hour and then cleaned in ethanol for 10 min. Then, unexposed resin inside the shell was cured for 60 min inside the UV Curing Chamber (XYZprinting).

The main elements of the experimental setup are shown in Fig. 4. A glass cell was closed by a specially designed sealing cap. The nozzle was mounted onto that cap. We established a negative gauge pressure inside the cell using a suction pump. Distilled water was injected with a syringe pump (KDS100, KD-Scientific). We controlled the helium flow with the pressure regulator of the bottle and verified that the loss of stagnation pressure in the gas circuit was less than 3%. We installed a mass flow meter (Flow Select F-201 CV) to determine the linear relationship $m' = 20\, p_0 - 2.0$ between the applied stagnation pressure p_0 (mbar) and the resulting mass flow rate m' (mg/min) for $0.3 \le p_0 \le 1.6$ bar. The upstream stagnation temperature and the temperature in the cell were measured with thermocouples. The pressure in the cell was measured with a gauge indicator.

Digital images of the liquid meniscus and jet were acquired at 10^5 fps using a high-speed video camera (Kirana-5M) equipped with optical lenses (Navitar 12X) and a microscope objective (10X Mitutoyo). The images consisted of 924×768 pixels. The magnification was 53×, which resulted in 0.56 μm/pixel. The camera could be displaced both horizontally and vertically using a triaxial translation stage with one of its horizontal axes motorized (Thorlabs Z825B) and controlled by the computer. The camera was illuminated with white backlighting and was triggered by an optical trigger (SI-OT3, Specialised Imaging). The optical trigger was

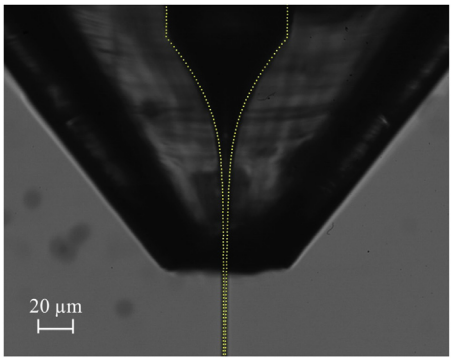

Fig. 5. Experimental image and free surface position calculated numerically (dotted line) for $p_0 = 1.75$ bar and $Q_l = 0.68$ ml/h.

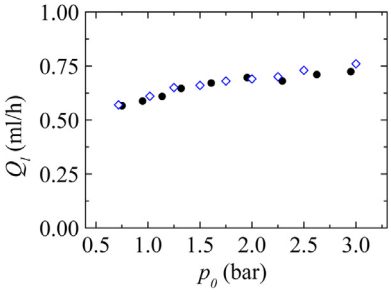

Fig. 6. Minimum value of the liquid flow rate Q_l as a function of the upstream stagnation pressure p_0 obtained experimentally (open symbols) and numerically (solid symbols).

equipped with optical lenses and illuminated with white backlighting. All the elements of the experimental setup were mounted on an optical table with a pneumatic anti-vibration isolation system to damp the vibrations coming from the building.

To determine the minimum flow rate, we first set the upstream stagnation pressure. Then, a relatively large liquid flow rate was injected through the feeding capillary. After a short transient regime, a steady liquid meniscus was formed attached to the feeding capillary edge. Finally, the liquid flow rate was reduced in steps of 0.01 ml/h until the jetting regime became unstable. Unfortunately, we could not obtain reliable measurements of the jet diameter for the extremely thin jets produced in our experiments. According to our estimations, the errors associated with the diffraction limit are of the order of 30%-50% for flow rates close to the critical value.

5. Results

Figure 5 shows the good agreement between the free surface shape in the experiment and that calculated with our numerical simulation for a quasi-marginally stable realization. This comparison should be taken with caution because the unknown optical distortion caused by the nozzle was not considered. The jet diameter in the simulation seems to be smaller than that obtained experimentally. However, it is difficult to determine the difference quantitatively due to the experimental uncertainty associated with the image's spatial resolution and the diffraction limit (the jet diameter is of the order of 1 μm). The minimum values of liquid flow rate Q_l obtained in the experiments are practically the same as those calculated from the global stability analysis (Fig. 6). As can be observed, the critical flow rate hardly depends on the upstream stagnation pressure for the range of values analyzed in this work, as occurs in the incompressible regime (Si et al., 2009; Montanero et al., 2011). This result may be expected because, as mentioned in Sec. 2, the increase of the stagnation pressure above the

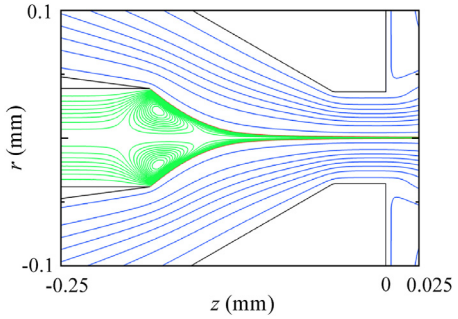

Fig. 7. Streamlines for $p_0 = 1.67$ bar and $Q_l = 0.75$ ml/h.

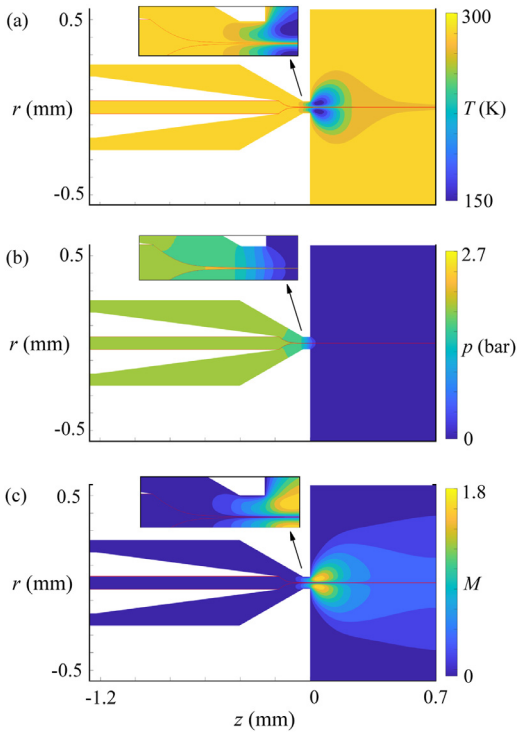

Fig. 8. Temperature (a), pressure (b) and Mach number (c) for $p_0 = 1.67$ bar and $Q_l = 0.75$ ml/h. The red line indicates the free surface position.

critical value leading to sonic choking hardly affects the viscosity force exerted by the gas stream on the free surface. The minimum flow rate can be significantly reduced only by appropriately changing the ejector geometry (for a fixed couple of fluids). It must be pointed out that unstable steady solutions are obtained as the liquid flow rate is decreased below the critical value. For this reason, the global linear stability analysis is required to determine the physically meaningful numerical realizations.

For the sake of illustration, Fig. 7 shows the streamlines for the quasi-marginally stable flow obtained for $p_0 = 1.67$ bar and $Q_l = 0.75$ ml/h. Similar results were obtained for other marginally stable cases. The major characteristic of the liquid flow pattern is the two counter-rotating recirculation cells in the liquid meniscus. As occurs in the incompressible case (Montanero et al., 2011; Cruz-Mazo et al., 2017; Mu et al., 2021), these cells arise for sufficiently low viscosity and liquid flow rate. Under these conditions, it has been speculated that the loss of stability of steady jetting is caused by the destabilization of those vortices (Montanero et al., 2011).

As can be observed in Fig. 8, both the gas and liquid temperature take homogeneous values in most of the fluid domain. However, the gas stream expands into the low-vacuum chamber at the

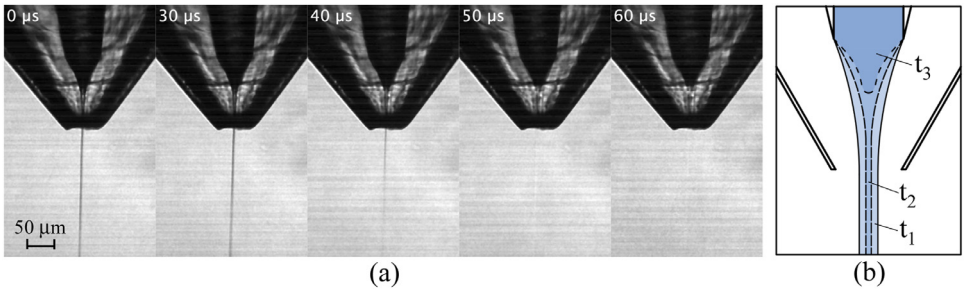

Fig. 9. (a) Sequence of images acquired when the liquid flow rate is decreased below its minimum value $Q_l = 0.69$ ml/h for $p_0 = 2$ bar. (b) Sketch to illustrate the free surface evolution during breakup.

nozzle exit, which causes a sharp drop in its temperature there. Despite the slenderness of the liquid jet, its temperature hardly decreases. This can be explained in terms of the low density of the surrounding gas and the small residence time of the liquid particle (Zahoor et al., 2018c). As can be observed in Fig. 8-b, there is a significant increase of the hydrostatic pressure in the tip of the liquid meniscus due to the accumulation of momentum in that region. This pressure increase makes the liquid flow back along the central part of the meniscus (Fig. 7). We plot in Fig. 8c the Mach number $M = v/a$, where v is the fluid velocity magnitude and a the sound speed. As expected, the flow is subsonic everywhere except in the nozzle exit, where transonic and supersonic conditions are reached.

In flow focusing, the outer gas stream stretches the liquid meniscus and sets in motion a certain volume of liquid. This volume must be continuously replaced by the liquid injection across the feeding capillary to reach steady conditions. The liquid meniscus tip inevitably thins and stops ejecting the liquid for injected flow rates lower than that dragged by the gaseous current. This instability mechanism is consistent with the images acquired in our experiments. Figure 9a shows a sequence of images acquired when the liquid flow rate is decreased below its minimum value. During the time interval $0 \le t \le 30$ μs, steady jetting is observed. For $30 \le t \le 50$ μs, both the meniscus tip and the emitted jet seem to collapse almost simultaneously, leaving a mark in the image corresponding to $t = 40$ μs. For $t \ge 50$ μs, the ejection does not take place, and the meniscus slightly retracts towards the feeding capillary. The dynamics of the system leading to the ejection interruption are sketched in Fig. 9b.

The free surface evolution is probably the best indicator of the mechanism responsible for the instability of flow focusing. In the global stability analysis, we assume the temporal dependence

$$F(z,t) = F_0(z) + \varepsilon f(z) e^{-i\omega t} \quad (\varepsilon \ll 1) \tag{10}$$

for the free surface position $F(z,t)$, where $F_0(z)$ stands for the steady free surface shape (see, e.g., the dotted line in Fig. 5). Figure 10 shows the magnitude of $f(z)$ for a marginally stable numerical solution. The real and imaginary parts of f are practically the same, which means that $F(z) - F_0(z) \simeq |f(z)| \sin(\omega_r t)$. This result implies that the perturbation corresponds to an oscillation with a constant phase shift of the entire free surface. This behavior may be explained in terms of the strong convective character of the system, which "synchronizes" the free surface deformation throughout the tapering meniscus and the emitted jet. The above result is consistent with the breakup dynamics observed in the experiments (Fig. 9), where both the meniscus tip and emitted jet seem to collapse simultaneously. We have verified that the above conclusions apply to the range of stagnation pressures analyzed in this work.

Due to the difficulties inherent to the fabrication of the flow focusing ejectors in SFX, numerical simulations have come up as

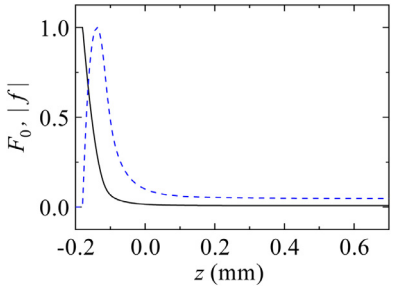

Fig. 10. Steady free surface position $F_0(z)$ (black solid line) and magnitude of the free surface perturbation, $|f(z)|$ (dashed blue line), for $p_0 = 1.6$ bar and $Q_l = 0.65$ ml/h. The curves have been normalized dividing by the corresponding maximum value.

a valuable alternative to search for the optimum ejector geometry (Sarler et al., 2021). The numerical method proposed in the present work is very useful for that purpose because it consumes much less computing time than any direct numerical simulation method. In this work, we calculated the minimum diameter $d_{\min}$ of the jet in the numerical domain as a function of the upstream stagnation pressure and liquid flow rate. We only considered stable realizations. It must be noted that $d_{\min}$ is expected to be smaller than the jet diameter at the nozzle exit due to the extra liquid acceleration caused by the gas stream in the discharge chamber.

Gañán Calvo et al. (2011) examined the deviation of the jet diameter from the scaling law (1) due to the liquid viscosity and the action of the tangential viscous stresses of the focusing gas in the incompressible regime. Following the same procedure, we here calculate the dimensionless diameter $d^*_{\min} \equiv d_{\min}/d_j$ to analyze the deviation of the jet diameter $d_{\min}$ from the value d_j given by the scaling law (1) (with $\Delta p = p_0 - p_e$). This deviation can be attributed to the gas compressibility and viscosity. For the purposes of dimensional analysis, it is convenient to formulate the problem in terms of the density $\rho_0 = p_0/(R_g T_0)$ instead of the temperature T_0. Then, the dimensionless diameter $d^*_{\min}$ can be expressed as

$$d^*_{\min} \equiv d_{\min}/d_j = f(\gamma, \mu_r, \kappa_r, \mathrm{Oh}_l; p_r, \rho_r, Q_r), \tag{11}$$

where $\gamma = c_p/c_v$, $\mu_r = \mu_g/\mu_l$, $\kappa_r = \kappa_g/\kappa_l$, $\mathrm{Oh}_l = \mu_l(\rho_l D\sigma)^{-1/2}$, $p_r = p_0/p_e$, $\rho_r = \rho_0/\rho_l$, $Q_r = Q_l/Q_D$, and $Q_D = D\mu_l/\rho_l$. In our numerical simulations, we fixed the values of the adiabatic constant γ, the viscosity and thermal conductivity ratios, μ_r and κ_r, and the Ohnesorge number Oh_l, while the values of p_r, ρ_r, and Q_r were changed.

In the incompressible regime (Gañán Calvo et al., 2011), the main contribution to the deviation f from unity must be assigned to Q_r, which controls the area where the gas exerts the viscous tangential stresses. We expect Q_r to affect significantly the value of f in the compressible regime as well. In addition, the influence of p_r on $d_{\min}$ is approximately taken into account in (11) through the diameter d_j given by (1). For this reason, we select ρ_r as the

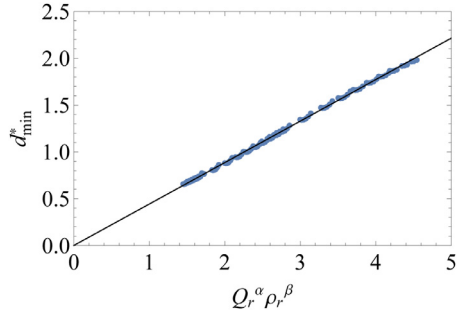

Fig. 11. $d^*_{\min} = d_{\min}/d_j$ versus $Q_r^{\alpha}\rho_r^{\beta}$ for $\alpha = 0.308$ and $\beta = -0.06$. The solid line is the function $y = 0.443x$.

remaining (subdominant) control parameter. Thus, we search for a scaling law of the form (Barenblatt, 2003)

$$d^*_{\min} = \mathcal{C}\, Q_r^{\alpha}\, \rho_r^{\beta}. \tag{12}$$

Using the optimization method described by Montanero and Gañán Calvo (2020), the best collapse of the numerical data around (12) is obtained for $\mathcal{C} = 0.433$, $\alpha = 0.308$ and $\beta = -0.06$ (Fig. 11). As expected, $\alpha \gg |\beta|$, which shows the dominant role of Q_r. The scaling law remarkably fits the numerical data in the range of values $0.549 \lesssim d_{\min} \lesssim 10.9$ μm calculated in our simulations.

The scaling law (12) implies that the jet's minimum diameter $d_{\min}$ and maximum velocity $v_{\max} = 4Q_l/(\pi d^2_{\min})$ scale as

$$d_{\min} \sim Q_l^{0.808} p_0^{-0.31}, \quad v_{\max} \sim Q_l^{-0.616} p_0^{0.19}, \tag{13}$$

respectively, when the ejector geometry, properties of the fluids, and stagnation temperature are fixed. The minimum liquid flow rate decreases with the stagnation pressure (Fig. 6) approximately as $Q_l \sim p_0^{0.18}$. Taking into account the scaling law (13), $d_{\min} \sim p_0^{-0.17}$ at the stability limit. This implies that thinner jets can be produced as p_0 increases even though the minimum flow rate slightly increases with p_0. As mentioned in Sec. 2, the variation of p_0 hardly affects the viscous stress exerted on the free surface under chocking flow conditions. Therefore, the term $p_0^{0.19}$ in Eq. (13) indicates that the drop of hydrostatic pressure contributes to the liquid acceleration as well.

6. Concluding remarks

We studied numerically and experimentally the transonic flow focusing used in SFX to place the sample into the beam focus. In the numerical analysis, the steady base flow was calculated as a function of the injected liquid flow rate and upstream gas stagnation pressure. Then, we solved the eigenvalue problem to obtain the linear global mode responsible for the steady jetting instability. In this way, we determined the minimum flow rate below which steady jetting cannot be reached.

Our results show that the minimum flow rate slightly depends on the stagnation pressure for the range of pressures considered in our analysis. This conclusion is similar to that obtained in the incompressible regime for sufficiently large pressure drops (Montanero et al., 2011). The simulation satisfactorily reproduces the shape of the experimental tapering meniscus. However, it seems to underestimate the jet diameter obtained experimentally.

Interestingly, the global stability analysis accurately predicts the minimum flow rate measured in the experiments. The agreement between the numerical and experimental results is even better than in the incompressible regime (Cruz-Mazo et al., 2017). The steady jetting interruption is caused by the growth of an inertio-capillary perturbation, making the meniscus and jet collapse simultaneously at the stability limit.

The scaling law for the jet diameter shows that the liquid flow rate is the most important control parameter, while the gas pressure (density) plays a secondary role. Equation (12) with $\alpha = 0.308$ and $\beta = -0.06$ is very accurate within the range of values $0.549 \lesssim d^*_{\min} \lesssim 10.9$ μm analyzed in the simulations. Significant deviations may be expected for other ejector geometries and higher liquid viscosities. These are probably the two major factors affecting the exponents in Eq. (12). The analysis of the influence of these factors will be the subject of future work.

Our numerical procedure consumes much less computing time than direct numerical simulations, in which the hydrodynamic equations are integrated over time until the jetting regime is established. For this reason, this procedure can be a helpful tool for determining the optimal parameter conditions in SFX. The major disadvantage of the present approach is that we cannot calculate the jet breakup length, which is an essential parameter in SFX. In fact, we cannot ascertain whether the minimum diameter $d_{\min}$ is attained before the jet breaks up. If that were the case, the scaling law (12) could not be used to calculate the diameter of the droplets resulting from the jet breakup.

To the best of our knowledge, transonic and supersonic flow focusing has been used only in SFX. The large liquid speed and the low pressure of the discharge chamber are not demanded in other existing applications and can constitute an obstacle for techniques such as fiber extruding or bioplotting. However, new applications will likely come up in the future to take advantage of the large kinetic energy of the emitted jet.

Declaration of Competing Interest

The authors declare that they have no known competing financial interests or personal relationships that could have appeared to influence the work reported in this paper.

CRediT authorship contribution statement

M. Rubio: Investigation. **A. Rubio:** Investigation. **M.G. Cabezas:** Supervision. **M.A. Herrada:** Software. **A.M. Gañán-Calvo:** Supervision. **J.M. Montanero:** Supervision, Writing - original draft.

Acknowledgements

This research has been supported by the Spanish Ministry of Science and Innovation under Grants PID2019-108278RB, by Junta de Extremadura under Grant GR18175, and by Junta de Andalucía under Grant P18-FR-3623. The authors are also grateful to P. Rodriguez-Díaz for her help in manufacturing the ejector.

References

Acero, A.J., Rebollo-Muñoz, N., Montanero, J.M., Gañán Calvo, A.M., Vega, E.J., 2013. A new flow focusing technique to produce very thin jets. J. Micromech. Microeng. 23, 065009.
Stan, C.A., et al., 2016. Liquid explosions induced by X-ray laser pulses. Nat. Phys. 12, 966–971.
Chapman, H.N., et al., 2011. Femtosecond X-ray protein nanocrystallography. Nature 470, 73–79.
Knoska, J., et al., 2020. Ultracompact 3D microfluidics for time-resolved structural biology. Nat. Commun. 11, 657.
Wiedorn, M.O., et al., 2018. Megahertz serial crystallography. Nat. Commun. 9, 4025.
Augello, L., Fani, A., Gallaire, F., 2018. The influence of the entry region on the instability of a coflowing injector device. J. Phys.: Condens. Matter 30, 284003.
Barenblatt, G.I., 2003. Scaling. Cambridge University Press, Cambridge, UK.
Beyerlein, K.R., Adriano, L., Heymann, M., Kirian, R., Knoska, J., Wilde, F., Chapman, H.N., Bajt, S., 2015. Ceramic micro-injection molded nozzles for serial femtosecond crystallography sample delivery. Rev. Sci. Instrum. 86, 125104.
Cabezas, M.G., Rubio, M., Rebollo-Muñoz, N., Herrada, M.A., Montanero, J.M., 2021. Global stability analysis of axisymmetric liquid-liquid flow focusing. J. Fluid Mech. 909, A10.

Gañán Calvo, A.M., 1998. Generation of steady liquid microthreads and micron-sized monodisperse sprays in gas streams. Phys. Rev. Lett. 80, 285–288.
Gañán Calvo, A.M., DePonte, D.P., Herrada, M.A., Spence, J.C.H., Weierstall, U., Doak, R.B., 2010. Liquid capillary micro/nanojets in free-jet expansion. Small 6, 822–824.
Gañán Calvo, A.M., Ferrera, C., Montanero, J.M., 2011. Universal size and shape of viscous capillary jets: application to gas-focused microjets. J. Fluid Mech. 670, 427–438.
Chomaz, J., 2005. Global instabilities in spatially developing flows. Annu. Rev. Fluid Mech. 37, 357–392.
Cruz-Mazo, F., Herrada, M.A., Gañán Calvo, A.M., Montanero, J.M., 2017. Global stability of axisymmetric flow focusing. J. Fluid Mech. 832, 329–344.
DePonte, D.P., Weierstall, U., Schmidt, K., Warner, J., Starodub, D., Spence, J.C.H., Doak, R.B., 2008. Gas dynamic virtual nozzle for generation of microscopic droplet streams. J. Phys. D: Appl. Phys. 41, 195505.
Dimakopoulos, Y., Tsamopoulos, J., 2003. A quasi-elliptic transformation for moving boundary problems with large anisotropic deformations. J. Comput. Phys. 192, 494–522.
Flynn, G.P., Hanks, R.V., Lemaire, N.A., Ross, J., 1963. Viscosity of nitrogen, helium, neon, and argon from −78.5° to 100°C below 200 atmospheres. J. Chem. Phys. 38, 154–162.
Gordillo, J.M., Sevilla, A., Campo-Cortés, F., 2014. Global stability of stretched jets: conditions for the generation of monodisperse micro-emulsions using coflows. J. Fluid Mech. 738, 335–357.
Herrada, M.A., Montanero, J.M., 2016. A numerical method to study the dynamics of capillary fluid systems. J. Comput. Phys. 306, 137–147.
Hirt, C.W., Nichols, B.D., 1981. Volume of Fluid (VOF) method for the dynamics of free boundaries. J. Comput. Phys. 39, 201–225.
Khorrami, M.R., 1989. Application of spectral collocation techniques to the stability of swirling flows. J. Comput. Phys. 81, 206–229.
Montanero, J.M., Gañán Calvo, A.M., 2020. Dripping, jetting and tip streaming. Rep. Prog. Phys. 83, 097001.
Montanero, J.M., Rebollo-Muñoz, N., Herrada, M.A., Gañán Calvo, A.M., 2011. Global stability of the focusing effect of fluid jet flows. Phys. Rev. E 83, 036309.
Mu, K., Qiao, R., Guo, J., Yang, C., Wu, Y., Si, T., 2021. Parametric study on stability and morphology of liquid cone in flow focusing. Int. J. Multiphase Flow 135, 103507.
Nazari, R., Zaare, S., Alvarez, R.C., Karpos, K., Engelman, T., Madsen, C., Nelson, G., Spence, J.C.H., Weierstall, U., Adrian, R.J., Kirian, R.A., 2020. 3D printing of gas–dynamic virtual nozzles and optical characterization of high-speed microjets. Opt. Express 28, 21749–21765.
Piotter, V., Klein, A., Plewa, K., Beyerlein, K.R., Chapman, H.N., Bajt, S., 2018. Development of a ceramic injection molding process for liquid jet nozzles to be applied for X-ray free-electron lasers. Microsyst. Technol. 24, 1247–1252.
Rubio-Rubio, M., Sevilla, A., Gordillo, J.M., 2013. On the thinnest steady threads obtained by gravitational stretching of capillary jets. J. Fluid Mech. 729, 471–483.
Sarler, B., Zahoor, R., Bajt, S., 2021. Alternative geometric arrangements of the nozzle outlet orifice for liquid micro-jet focusing in gas dynamic virtual nozzles. Materials 14, 1572.
Sauter, U.S., Buggisch, H.W., 2005. Stability of initially slow viscous jets driven by gravity. J. Fluid Mech. 533, 237–257.
Shapiro, A.H., 1953. Compressible fluid flow. John Wiley and Sons Inc., New York, USA.
Si, T., Li, F., Yin, X.Y., Yin, X.Z., 2009. Modes in flow focusing and instability of coaxial liquid-gas jets. J. Fluid Mech. 629, 1–23.
Tammisola, O., Lundell, F., Soderberg, L.D., 2012. Surface tension-induced global instability of planar jets and wakes. J. Fluid Mech. 713, 632–658.
Theofilis, V., 2003. Advances in global linear instability of nonparallel and three-dimensional flows. Prog. Aerosp. Sci. 39, 249–315.
Theofilis, V., 2011. Global linear instability. Annu. Rev. Fluid Mech. 43, 319–352.
Vega, E.J., Montanero, J.M., Herrada, M.A., Gañán Calvo, A.M., 2010. Global and local instability of flow focusing: The influence of the geometry. Phys. Fluids 22, 064105.
Zahoor, R., Bajt, S., Sarler, B., 2018. Influence of gas dynamic virtual nozzle geometry on micro-jet characteristics. Int. J. Multiphase Flow 104, 152–165.
Zahoor, R., Bajt, S., Sarler, B., 2018. Numerical investigation on influence of focusing gas type on liquid micro-jet characteristics. Int. J. Hydromechatronics 1, 222–237.
Zahoor, R., Belsak, G., Bajt, S., Sarler, B., 2018. Simulation of liquid micro-jet in free expanding high-speed co-flowing gas streams. Microfluidics and Nanofluidics 22, 87.
Zahoor, R., Regvar, R., Bajt, S., Sarler, B., 2020. Simulation of liquid micro-jet in free expanding high-speed co-flowing gas streams. Microfluidics and Nanofluidics 20, 71–83.